THE JOURNAL OF PHYSICAL CHEMISTRY C

Article

pubs.acs.org/JPCC

Hydrogen and Electric Power Generation from Liquid Microjets: Design Principles for Optimizing Conversion Efficiency

Nadine Schwierz,[*,†,§] Royce K. Lam,[†,‡,§] Zach Gamlieli,[†] Jeremiah J. Tills,[†] Alvin Leung,[†] Phillip L. Geissler,[†,‡,¶] and Richard J. Saykally[*,†,‡]

[†]Department of Chemistry, University of California, Berkeley, California 94720, United States

[‡]Chemical Sciences Division, Lawrence Berkeley National Laboratory, Berkeley, California 94720, United States

[¶]Materials Sciences Division, Lawrence Berkeley National Laboratory, Berkeley, California 94720, United States

ABSTRACT: Liquid water microjets have been successfully employed for both electrical power generation and gaseous hydrogen production, but the demonstrated efficiencies have been low. Here, we employ a combination of a modified Poisson−Boltzmann description, continuum hydrodynamic equations, and microjet electrokinetic experiments to gain detailed insight into the origin of the streaming currents produced in pure water. We identify the contributions to the streaming current from specific ion adsorption at the solid/liquid interface and from long-ranged electrostatic interactions, finding that the portion originating from the latter dominate at charged surfaces. The detailed understanding afforded by theory and the close agreement with experimental results elucidates design principles for optimizing hydrogen production and power generation. Changing the sign of the surface charge density through targeted use of surface coatings via silanization switches the primary charge carrier between hydronium and hydroxide and therefore switches the corresponding production of molecular hydrogen to oxygen at the target electrode. Moreover, hydrophobic surface coatings reduce dissipation due to fluid/solid friction, thereby increasing the conversion efficiency.

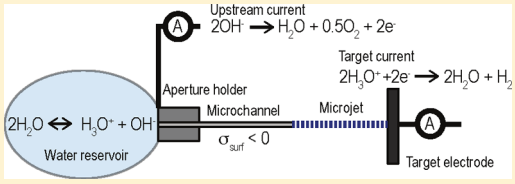

INTRODUCTION

Micro- and nanofluidic devices have shown promise for energy conversion and have received significant attention over the past few years. For instance, electrokinetic currents can be produced by forcing water through porous materials or through well-defined micron- or nanometer-sized channels.[1−18] Liquid microjet electrokinetics allow for the conversion of hydrostatic pressure directly into electrical energy and molecular hydrogen and also increase the conversion efficiency (>10%) by eliminating back conduction due to electroosmotic flow.[1,2] Xie et al. have recently reported up to 48% efficiency in the conversion of kinetic energy to potential energy for a droplet train driven into a strong electric field.[19]

It has long been recognized that streaming currents arise from the asymmetric distribution of anions and cations in an interfacial electric double layer. At charged interfaces, this double layer is formed from electrostatic interactions of the ions with the charged surface. Specific ion adsorption or repulsion at a solid/electrolyte interface also contributes to the asymmetric charge distribution, leading to anomalous ion-specific electrokinetic effects in uncharged channels.[20] However, the question of whether the streaming current in pure water results from the selective adsorption of hydroxide ions to a solid interface,[1] or whether the electrostatic interactions of hydronium and hydroxide with surface charges might play an important role, has not yet been addressed.

We employ a combination of modified Poisson−Boltzmann (PB) theory, including nonelectrostatic ion−surface interactions, continuum hydrodynamics, and microjet electrokinetic measurements to identify the origin of the streaming current. This approach identifies the contributions to the streaming current from long-ranged electrostatic interactions and specific adsorption of hydronium and hydroxide at the solid/liquid interface. At charged surfaces, the contribution from long-ranged electrostatic interactions results in streaming currents that are significantly larger than those induced by specific ion adsorption to uncharged interfaces. The detailed understanding afforded by this theory and the close match between the theoretical and the experimental results allows us to adjust surface properties and apparatus design to optimize power generation and conversion efficiency. In particular, targeted functionalization of the microjet surface via silanization is used to vary the surface charge density and the surface hydrophobicity. Changing the sign of the surface charge reverses the sign of the streaming current and switches between hydronium and hydroxide as the primary charge carrier and therefore between the production of molecular hydrogen or oxygen. Additionally, increasing the surface hydrophobicity reduces energy loss resulting from fluid/surface frictional forces, thereby increasing the conversion efficiency.

METHODS

A. Streaming Current for Liquid Microjets. Electrokinetic streaming currents originate from the overlap between

Received: April 13, 2016
Revised: June 8, 2016
Published: June 9, 2016

DOI: 10.1021/acs.jpcc.6b03788
J. Phys. Chem. C 2016, 120, 14513−14521

the fluid velocity profile with the charge distribution at solid/liquid interfaces. For a charged or biased surface, an electric double layer forms as counterions are attracted to the surface, while similarly charged ions are repelled. In addition, specific ion adsorption or depletion at the interface contributes to the ionic distribution. The latter can lead to the formation of an electric double layer at an uncharged surface if the anions and the cations have unequal surface affinities and thereby induce ion-specific electrokinetic effects in uncharged channels. Quantitatively, the streaming current in a circular channel of radius R can be calculated from the integral of fluid velocity profile $v(z)$ and the net charge distribution $\rho(z)$

$$I = \int_0^R v(z)\rho(z)2\pi(R - z)\,\mathrm{d}z \tag{1}$$

where $z = R - r$ is the distance from the channel wall. The net charge density $\rho(z)$ is the sum of the individual ion number densities

$$\rho(z) = \sum_i q_i n_i(z) \tag{2}$$

In pure water, $n_i(z)$ corresponds to the number densities of hydronium and hydroxide from autoionization with a bulk concentration of 10^{-7} M. The distribution of the ions in the channel is obtained from the analytical solution of a modified Poisson−Boltzmann equation in a flat plane approximation, as detailed further below. Note that the liquid microjet employed in our experimental design breaks up into droplets (via Rayleigh instabilities) before reaching the target electrode thereby disrupting the system's electrical continuity and eliminating back conduction. Therefore, electroosmotic flow is not included in the present theoretical description.

In the following, we consider the two flow profiles that arise in our experimental designs, top hat flow and laminar flow. The characteristic length scale L_c over which flow profile develops is[21]

$$L_c/(2R) \approx 0.06R_e \text{ (laminar flow)},$$
$$L_c/(2R) \approx 4.4R_e^{1/6} \text{ (turbulent flow)} \tag{3}$$

where R_e is the Reynolds number, the ratio between the inertial forces to the viscous forces, defined as

$$R_e = \frac{2R\bar{v}\rho_W}{\eta_W} \tag{4}$$

where $\bar{v}$ is the bulk velocity and ρ_W and η_W are the density and viscosity of water, respectively.

For our Pt/Ir aperture, a channel length L of 0.09−0.12 mm is insufficient for developing either completely turbulent or laminar flow at sufficiently high flow velocities. The velocity profile comprises a laminar sublayer close to the metal wall of thickness δz in which the fluid velocity increases linearly until it reaches the bulk fluid velocity.[22,23] The resulting top hat velocity profile is given by

$$v_x(z) = \begin{cases} \bar{v}z/\delta z & \text{for } z < \delta z \\ \bar{v} & \text{otherwise} \end{cases} \tag{5}$$

with a laminar sublayer thickness $\delta z = 116RR_e^{-7/8}$. For our silica capillary channels, a channel length of 1−1.5 cm is sufficient for developing laminar flow. Under these conditions, the velocity profile is given by

$$v_x(z) = \frac{\Delta p}{4\eta_W L}(2Rz - z^2) \tag{6}$$

where Δp is the pressure differential between the inlet and outlet. In both cases, the average fluid velocity v follows from the volumetric flux

$$Q = v\Omega = \int_\Omega v(z)\,\mathrm{d}a \tag{7}$$

where Ω is the cross sectional area of the channels.

B. Streaming Current in the Limit of Large Diameter Channels ($\kappa R \gg 1$). If the channel diameter is large compared to the width of the electrostatic double layer ($\kappa R \gg 1$), the streaming current can be approximated as[22,24]

$$I = -4\pi v_0 \epsilon\zeta \text{ (laminar flow)},$$
$$I = -\frac{2\pi\bar{v}\epsilon R\zeta}{\delta z} \text{ (top hat flow)} \tag{8}$$

where ζ is the zeta potential. Commonly, ζ is interpreted as the electrostatic potential at the shear plane, the position near the wall where the hydrodynamic flow velocity vanishes.[25] From here forward, we cease using the empirical description in terms of the zeta potential. Instead, we make use of the Navier boundary condition to quantitatively account for the effect of surface slippage on ion transport. Consequently, the fluid velocity results from a balance between the driving force induced by applying a pressure differential along the channel and the viscous frictional forces on the surface, as discussed in more detail below. Note that in pure water, the Debye length κ^{-1}, corresponding to the characteristic double layer thickness, is 0.974 μm. As a result, eq 8 is only valid for channels much larger than employed in our current design or for higher bulk salt concentrations.

C. Slip Length and Surface Friction. The slip length l_b characterizes the hydrodynamic boundary condition of the fluid at the confining surface. It is defined by[26]

$$l_b\partial_z v_x(z) = v_x(z) \tag{9}$$

where $v_x(z)$ is the tangential fluid velocity field. The slip length is a measure of the friction of the fluid at the interface, where larger slip lengths are associated with lower surface friction. Experiments and theoretical predictions indicate that the slip length depends critically on the surface wettability measured by the water contact angle.[27,28] Depending on surface hydrophobicity, typical values for the slip length range from a few tens of nanometers for hydrophobic surfaces to negative values of similar magnitude for hydrophilic surfaces. The negative slip length at hydrophilic surfaces is important for modeling surface conductivities when specific ion adsorption is considered.[29] As such, tuning the surface hydrophobicity provides an avenue for modifying the microfluidic and charge transport properties of a substrate. At a solid/water interface, the following relation between the water contact angle Θ and the slip length l_b has been obtained from atomistic MD simulations[27,28]

$$l_b = 0.63 \text{ nm}\cdot(1 + \cos\Theta)^2 \tag{10}$$

Taking slippage effects into account by applying the Navier boundary condition (eq 9) for laminar flow, yields

$$v(z) = \frac{\Delta p}{4\eta_W L}(2l_bR + 2Rz - z^2) \tag{11}$$

DOI: 10.1021/acs.jpcc.6b03788
J. Phys. Chem. C 2016, 120, 14513−14521

The dissipation associated with the fluid/solid friction is[30]

$$P_{\text{diss}} = \frac{128Q^2\eta L}{\pi(16R^4 + 64l_bR^3)} \tag{12}$$

Increasing the slip length reduces energy dissipation and provides a major advantage when using large arrays of microchannels for energy conversion or desalination. Moreover, in carbon nanotubes, the slip length can be 2 orders of magnitude larger than in other hydrophobic channels and even larger than the diameter of the nanotubes.[31] Miniaturization of our microchannels toward nanometer sized channels is therefore especially promising as the energy dissipation scales inversely with the slip length.

D. Solution of the Linearized Poisson−Boltzmann Equation Including Specific Ion−Surface Interactions. The ionic distribution in the microchannels is derived from a 1D modified Poisson−Boltzmann equation.[32,33] Ion−surface interactions are explicitly included by choosing square-well potentials for the interaction between the ions and the surface

$$V_i(z) = V_{i0}\Theta(b_i - z) \tag{13}$$

Here, V_{i0} corresponds to the ionic surface affinity for ions of type i, b_i is the interaction range, and $\Theta(b_i - z) = 1$ for $z < b_i$ and $\Theta(z) = 0$ otherwise. Since the full PB equation including specific ion adsorption can only be solved quasi-analytically,[34] we have restricted the scope of our current model to small bulk salt concentrations and low ion−surface affinities. For $q\Phi \ll k_BT$, the PB equation can be linearized

$$\frac{d^2\Phi(z)}{dz^2} = -\sum_i \frac{q_i c_{i0} a_i(z)}{\epsilon}\left(1 - \frac{q_i\Phi(z)}{k_BT}\right) = \kappa'(z)^2\Phi(z) - J(z) \tag{14}$$

where z is the distance perpendicular to the interface, q_i is the charge of ions of type i, c_{i0} the bulk salt concentration for ionic species i, $\Phi(z)$ the local electrostatic potential, and ϵ the dielectric constant of water. Ion-specificity is accounted for by $a_i(z) = e^{-V_i(z)/k_BT}$, which depends on the ion−surface potentials $V_i(z)$ that are, in general, different for cations and anions. Assuming identical interaction ranges for cations and anions, $b^+ = b^- = b$, eq 14 can be solved piecewise in regions I and II corresponding to the regions of finite or vanishing ion−surface interaction. The modified inverse Debye screening length κ' is defined as

$$\kappa'(z)^2 = \frac{1}{\epsilon k_BT}\sum_i q_i^2 c_{i0} a_i(z) = \begin{cases} \kappa_I^2; & z < b \\ \kappa_{II}^2; & z > b \end{cases} \tag{15}$$

and the parameter J is defined as

$$J(z) = \frac{1}{\epsilon}\sum_i q_i c_{i0} a_i(z) = \begin{cases} J_I; & z < b \\ J_{II}; & z > b \end{cases} \tag{16}$$

Equation 14 can be integrated twice yielding

$$\frac{1}{\kappa'}\left(\ln\left(2\left(-J + \kappa'^2\Phi + \kappa'\sqrt{C_1 - 2J\Phi + \kappa'^2\Phi^2} + K_2\right)\right)\right) = z \tag{17}$$

where C_1 and K_2 are the integration constants. The solution must satisfy the following boundary conditions (BCs):

$$\text{(i)}\ \left.\frac{d\Phi_I(z)}{dz}\right|_{z=0} = \Sigma \tag{18}$$

$$\text{(ii)}\ \left.\frac{d\Phi_{II}(z)}{dz}\right|_{z=R} = 0 \tag{19}$$

$$\text{(iii)}\ \left.\frac{d\Phi_I(z)}{dz}\right|_{z=b} = \left.\frac{d\Phi_{II}(z)}{dz}\right|_{z=b} \tag{20}$$

$$\text{(iv)}\ \Phi_I(z)|_{z=b} = \Phi_{II}(z)|_{z=b} \tag{21}$$

with $\Sigma = -\sigma/\epsilon$ where σ is the surface charge density. The matching conditions (iii) and (iv) are used to provide a continuously differentiable potential at b. The electrostatic potential is thereby defined as

$$\Phi_I(z) = \frac{1}{4\kappa_I^2}(C_{2I}\, e^{-\kappa_I z} - 4\, e^{-\kappa_I z}\Sigma\kappa_I + 4J_I + C_{2I}\, e^{\kappa_I z}) \tag{22}$$

$$\Phi_{II} = \frac{(e^{\kappa_{II}(2R-z)}C_{2II} + 4J_{II} + C_{2II}\, e^{\kappa_{II}z})}{4\kappa_{II}^2} \tag{23}$$

Note that for large channels, the potential vanishes and eq 23 reduces to $\Phi_{II}(z) = C_{II}^{DH}\, e^{-\kappa z}$. Applying the boundary conditions yields

$$C_{2I} = -\frac{-4\kappa_{II}^2\, e^{-\kappa_I b}\Sigma\kappa_I + 4\kappa_{II}^2 J_I - \kappa_I^2\, e^{-\kappa_{II}(-2R+b)}C_{2II} - 4\kappa_I^2 J_{II} - \kappa_I^2 C_{2II}\, e^{\kappa_{II}b}}{\kappa_{II}^2(e^{-\kappa_I b} + e^{\kappa_I b})} \tag{24}$$

$$C_{2II} = \frac{4(\kappa_{II}^2\, e^{-\kappa_I b}J_I - e^{-\kappa_I b}\kappa_I^2 J_{II} + 2\kappa_{II}^2\, e^{-\kappa_I b}\Sigma\kappa_I\, e^{\kappa_I b} - e^{\kappa_I b}\kappa_{II}^2 J_I + e^{\kappa_I b}\kappa_I^2 J_{II})}{\kappa_I((\kappa_I - \kappa_{II})\, e^{2\kappa_{II}R - \kappa_{II}b - \kappa_I b} - (\kappa_I\kappa_{II})\, e^{2\kappa_{II}R - \kappa_{II}b + \kappa_I b} + (\kappa_I + \kappa_{II})\, e^{-b(\kappa_I - \kappa_{II})} - (\kappa_I - \kappa_{II})\, e^{b(\kappa_{II} + \kappa_I)})} \tag{25}$$

The concentration profiles of the ith ionic species is calculated from

$$c_i(z) = c_{i0}a_i(z)(1 - q_i\Phi(z)/k_BT) \tag{26}$$

with the bulk ion concentration c_{i0}.

E. Parameterization of Specific Interactions of Hydronium and Hydroxide with a Channel Surface. Specific ion adsorption at a hydrophobic surface has been shown to accurately explain experimental data for long-ranged interactions between silica surfaces in different salt solutions.[35,36] As such, we have used the abundant data for the interfacial tension

DOI: 10.1021/acs.jpcc.6b03788
J. Phys. Chem. C 2016, 120, 14513−14521

at the air/water interface to parameterize the interfacial affinity of hydronium and hydroxide at water/silica interface, thereby capturing the ionic excess and the partitioning of the ions in the interfacial region. Within a mean field approximation, the interfacial tension can be written in terms of the electrostatic potential and the ionic concentration as

$$\Delta\gamma(V_0^{\pm}, c_0) = \int_0^{\infty}\left[\frac{1}{2}(c^+(z) - c^-(z))q\Phi(z)\right]dz + k_BT\int_0^{\infty}\left[c^+(z)\ln\frac{c^+(z)}{c_0} + c^-(z)\ln\frac{c^-(z)}{c_0} + \Delta c(z)\right]dz + \int_0^{\infty}[V^+(z)c^+(z) + V^-(z)c^-(z)]\,dz \quad (27)$$

where the first integral is the electrostatic energy, the second integral represents the ideal mixing entropy of a dilute solution of anions and cations, and the last integral accounts for the ion−surface interaction.[34,37,38] However, the free energy expression (eq 27) that is used here does not directly yield the relation between the electrostatic potential and the ionic densities via minimization, as the two fields depend implicitly on each other via the Poisson−Boltzmann equation. Note that the expression used is more convenient for our analytical solution than the expression from Borukhov et al.[37,38] and can be applied here as both the potential and the densities are known. Approximating $\ln\frac{c^+(z)}{c_0} \approx \ln a_{\pm}(z) - q\Phi/k_BT$ yields a closed form expression for the free energy per unit area. From this expression, the ion−surface interaction strength $V^{\pm}$ is chosen such that it reproduces the experimental air/electrolyte surface tension for a 100 mM solution (Figure 1).[39] We have

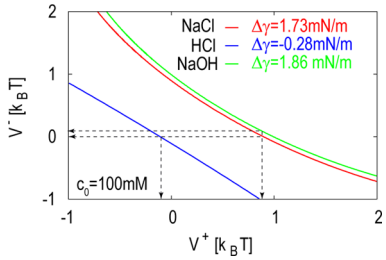

Figure 1. Optimal values for anion and cation surface interaction strength $V^{\pm}$. The lines correspond to the combination of V^+ and V^- that reproduces the experimental air/electrolyte surface tension for 100 mM bulk salt concentration (given as inset). The arrows indicate our choice of ion−surface interaction parameters with chloride as reference ($V^{Cl^-} = 0$).

chosen the interfacial binding affinity of chloride as the reference ($V^{Cl^-} = 0$). This choice is motivated by vanishing ion specific electrokinetic effects in NaCl solutions.[20] The corresponding binding affinity for the cation V^+ is then determined from relationships represented in Figure 1. The interaction range for anions and cations is chosen to be $b^+ = b^- = 1$ nm, based on the results from molecular dynamics simulations.[34,40] In our model, H_3O^+ is slightly surface accumulated (with surface binding affinity $V^+ = -0.11k_BT$), while OH^- is weakly excluded ($V^- = +0.08k_BT$). While the partitioning of hydronium and hydroxide at the air/water interface has been actively debated in recent literature,[41] our model is in agreement with the salt partitioning model for the air/water interface by Pegram and Record,[42] classical and *ab initio* molecular dynamics simulations,[43−45] nonlinear spectroscopic studies,[46,47] and X-ray photoelectron spectroscopy measurements.[48] Conversely, the preferential adsorption of hydroxide to the air/water interface has been suggested by electrophoresis,[49] titration,[50] and mass spectrometry measurements.[51] Some theoretical studies have also indicated that the difference between the surface propensities of hydronium and hydroxide is small.[52]

F. Electrokinetic Apparatus. The microjet electrokinetics apparatus used here has been described in previous publications.[1,2,53] Briefly, a high pressure liquid chromatography (HPLC) pump drives the liquid through PEEK tubing into a 30 μm inner diameter fused silica capillary. Electrokinetic currents were measured both "upstream," through the stainless steel fitting that holds the capillary, and "downstream," via a copper target electrode, using Keithley 428 and FEMTO DDPCA-300 current amplifiers. Water, with a resistivity of 18.2 MΩ·cm, used in the experiments was obtained from a Millipore purification system. Glassware was acid cleaned regularly with a Nochromix/sulfuric acid solution and rinsed with purified water.

G. Jet Coatings. The fused silica capillary tubing was functionalized using commercially available organosilanes. Trimethoxy(octadecyl)silane (ODS) [Technical grade, 90%] and (3-aminopropyl)triethoxysilane (APTES) [99%] were obtained from Sigma-Aldrich. *N*,*N*-Didecyl-*N*-methyl-(3-trimethoxysilylpropyl)-ammonium chloride (DDMAC) [40−42% in methanol] and octadecyldimethyl(3-trimethoxysilylpropyl)-ammonium chloride (DMOAP) [60% in methanol] were obtained from Gelest. The capillary tubing was cut to 1.5 cm and soaked in solutions of 20 mM total organosilane concentration in toluene for 2−4 h. To facilitate the reaction, a small amount of water was added to the mixtures. The capillaries were then removed from solution and baked for ∼6 h at 140 °C.

RESULTS AND DISCUSSION

In this work, we investigate electrokinetic streaming currents generated from water flowing through micrometer-sized channels by combining a modified Poisson−Boltzmann description and continuum hydrodynamic equations with results from microfluidic experiments. Figure 2A summarizes our current understanding of the origin of a streaming current in a negatively charged channel. For the silica and PtIr channels used in the experiments, the negative surface charge arises from the dissociation of the silanol or metal oxide groups in water. In pure water, the streaming current originates from charge separation between hydronium and hydroxide. At the negatively charged walls, a pronounced double layer is formed, with a thickness of ∼1 μm. Hydronium is attracted to the interface, while hydroxide is repelled (Figure 2B). The distribution of the ions is dominated by long-ranged electrostatic interactions with the charged channel walls, while nonelectrostatic ion−surface interactions play only a minor role due to the low surface affinities of hydronium and hydroxide ($V^+ = -0.11k_BT$, $V^- = +0.08k_BT$). Consequently, the electrostatic potential is negative and decays exponentially with increasing distance from the channel walls (Figure 2C). The charge flux, resulting from the overlap between the net charge density and the laminar flow profile (Figure 2D), originates in the double layer region, in which the distribution of hydronium and hydroxide is unequal, and extends several microns into the channel due to the low screening in pure water (Figure 2E). As a result of the extended double layer, hydronium is

DOI: 10.1021/acs.jpcc.6b03788
J. Phys. Chem. C 2016, 120, 14513−14521

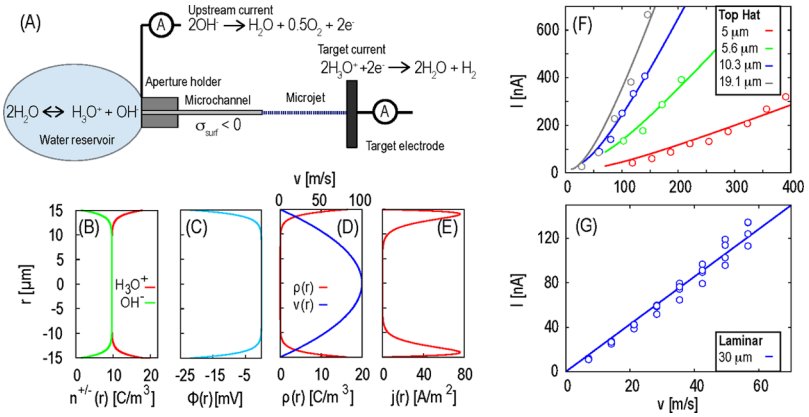

Figure 2. (A) Experimental design of the liquid microjet electrokinetics apparatus. (B) Density profiles of hydronium and hydroxide in pure water for a 30 μm channel with bare surface charge density $\sigma = -0.0001$ e/nm^2. (C) Electrostatic potential. (D) Charge density and flow velocity profile for laminar flow. (E) Charge flux $j(r) = \rho(r)v(r)$. (F) Streaming current as a function of the average flow velocity for top hat flow and different PtIr channel diameters from electrokinetic measurements (open circles, adapted from refs 1 and 2, discarding data points that are not in the regime of top hat flow) and theoretical predictions (lines). (G) Streaming current for laminar flow in a 30 μm silica channel from experiments (open circles) and theory (lines).

Table 1. Surface Properties of the Microchannels: Material, Surface Charge Density (σ), and Surface Potential (Φ_0) Based on Our Theoretical Model[a]

material	flow condition	diameter [μm]	σ [e/nm^2]	Φ_0 [V]	ref
PtIr	top hat	5–19.1	-0.001 ± 0.0002	-0.22 ± 0.04	1,2
silica	laminar	30	$-0.00067 \pm 2.7 \cdot 10^{-5}$	-0.15 ± 0.006	current work
silica			-0.00055 to -0.00083		54

[a]A reference to the experimental data used for the prediction is given in the last column.

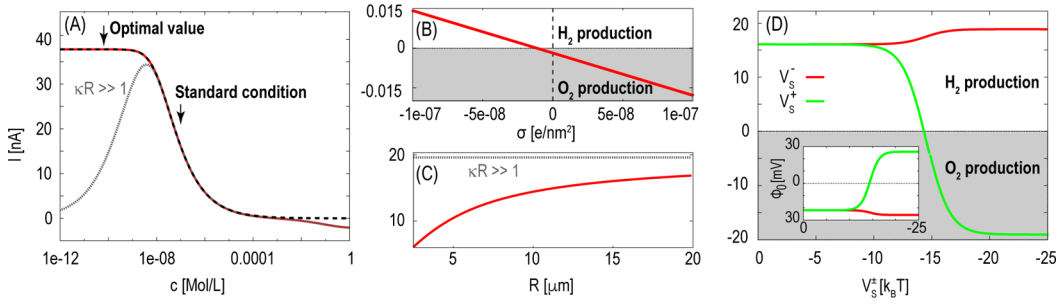

Figure 3. Streaming current (nA) as a function of different parameters for a 30 μm channel with an average flow velocity $v = 50$ m/s. Unless otherwise stated, the channel has a surface charge density of $\sigma = -0.0001$ e/nm^2: (A) Streaming current dependence on the bulk ion concentration (red line). The dotted line indicates the limit in which the electric double layers do not overlap (large channels). The dashed line is the result for neglecting specific ion adsorption at the liquid/solid interface. (B) Streaming current dependence on the surface charge density. The value of the anomalous streaming current for uncharged channels is -1.8 pA. (C) Streaming current dependence on the channel radius. The dotted gray line indicates the frequently used approximation in the limit $\kappa R \gg 1$ (eq 8). (D) Streaming current dependence on the anion or cation ion–surface affinity $V_S^{\pm}$ for a 0.1 nM salt solution. The electrostatic surface potential (Φ_0) is shown in the inset. Gray areas indicate reversal of the sign of the streaming current leading to oxygen production at the target electrode.

preferentially sheared away. At the target electrode, the unbalanced protons extract electrons to produce molecular hydrogen, as confirmed in our previous work.[1] The excess hydroxide in the reservoir discharges at the upstream nozzle connected to the reservoir and generates oxygen (Figure 2A).

Figure 2F,G show the dependence of the streaming current on the average flow velocity obtained from experiments under top hat and laminar flow conditions (open circles) compared to the theoretical predictions using the surface charge density as the only adjustable parameter (lines). The resulting values for the surface charge density and electrostatic surface potential are summarized in Table 1. Our results are in good agreement with those measured for silica by Behrens et al.[54]

Under top hat flow conditions, the streaming current scales as $v^{15/8}$ in the limit where $\kappa R \gg 1$, while under laminar flow, the streaming current increases linearly with v. This provides a method for discriminating between different flow conditions. Overall, our theoretical model provides an excellent description of the experimental results under different flow conditions for small channels with low ionic strength ($\kappa R \approx 1$). Moreover, the model provides detailed insight into the ionic distribution and the electrostatic potential (Figure 2) and can be used to predict the surface charge density and the surface potential. Note, however, that the analytical description is limited to $q\Phi \ll k_BT$. To accurately estimate the charge density of highly charged surfaces, numerical solutions of the full PB equation should be applied. In the following, we therefore restrict the discussion to

DOI: 10.1021/acs.jpcc.6b03788
J. Phys. Chem. C 2016, 120, 14513–14521

low surface charge densities, wherein an analytical solution for the streaming current exists. This solution permits modeling of the influence of the surface and electrolyte properties over a wide range of parameters, which is essential to deriving the design principles necessary for maximizing power and hydrogen generation. In particular, we focus on the effect of the electrolyte concentration, the magnitude and sign of the surface charge density, the channel diameter, and the surface hydrophobicity under laminar flow conditions.

Figure 3A shows the streaming current's dependence on the ion concentration. At small ion concentrations, the streaming current has a plateau that scales as $I \propto R\sigma v$ in the limit of vanishing ion concentration. The current is maximized if the double layers from each side of the channel overlap and the full cross-section of the channel contributes to charge separation. With increasing ion concentration, the double layer and therefore the region that contributes to the streaming current decreases due to increased screening. At large ion concentrations, where the screening length is on the order of the nonelectrostatic ion−surface interaction range, specific ion adsorption at the channel walls becomes important. Here, excess adsorbed hydronium at the channel walls results in a surface charge reversal from negative to positive. As a result, hydroxide ions are attracted to the channel walls and form a second adsorption peak (data not shown). In this case, both hydronium and hydroxide ions are sheared away, leading to a slightly negative streaming current (∼5 nA) due to the predominant flux of hydroxide ions. Moreover, at an uncharged surface in pure water under standard conditions (with bulk concentration $c_0 = 10^{-7}$ M of hydronium and hydroxide), the streaming current resulting from specific adsorption amounts to −1.8 pA (Figure 3B). This ion-specific "anomalous" streaming current is closely related to the electroosmotic flow at uncharged hydrophobic channels in sodium iodide solutions.[20] The contribution to the streaming current from specific adsorption of hydronium and hydroxide to an uncharged surface is minor. However, it can become important for strong ion−surface interactions at charged surfaces, as will be discussed further below. For a small negative surface charge ($\sigma = 1.2 \times 10^{-8}$ e/nm^2), the effect of preferential hydronium adsorption can be exactly canceled (point of zero charge). Beyond this point, the streaming current is positive and increases linearly with increasing negative surface charge. The situation is reversed if the sign of the surface charge density is reversed. In this case, the streaming current is negative since hydroxide is attracted to the positively charged channel walls and sheared away preferentially, leading to oxygen production at the target electrode.

Figure 3C shows the dependence of the current on the channel size. Similar to the results for top hat flow (Figure 2F), the streaming current increases with increasing channel size at a given flow velocity. The dashed line indicates a frequently used approximation in the limit $\kappa R \gg 1$.[24]

In addition to electrical and hydrogen generation, our apparatus can be used to detect small changes in surface properties resulting from the selective interaction of different ions with surfaces in ultradilute solutions.[53] In Figure 3D, we show the effects of adding 0.1 nM anions and cations with surface affinity $V_S^{\pm}$ while maintaining a constant concentration of hydronium and hydroxide. The streaming current is affected only for ion−surface interactions much larger than the thermal energy k_BT. Strong anion adsorption creates a higher effective surface charge and therefore generates greater charge separation and a larger streaming current. Strong cation adsorption, however, reduces the effective surface charge density and therefore decreases the streaming current. For instance, the addition of 0.1 nM KCl leads to a 10% reduction in the streaming current.[53] This corresponds to a cation affinity of about $V_S^{+} = 12k_BT$, which is similar in magnitude to the nonelectrostatic affinity of cations to carboxylate surface groups.[55] Consequently, ultradilute experiments allow us to estimate the affinity of cations to the surface silanol groups. The affinity of the ions for the undissociated silica surface groups is too weak ($<10k_BT$) to affect the streaming current at such low salt concentrations.[34]

In addition to surface charge and channel dimensions, the hydrophobicity of the channel walls plays an important role for the energy conversion efficiency. While the former conditions mainly influence the ionic distribution, the surface hydrophobicity has a direct influence on the hydrodynamic flow profile. On small scales, the hydrodynamic boundary conditions deviate from the usual nonslip boundary condition. Assuming that the surface stress is linearly related to the surface velocity leads to the slip length shown schematically in the inset of Figure 4A.[56] Increasing the surface slip by increasing the hydrophobicity enhances the flow rate through small channels, offering the possibility of reducing dissipation due to fluid/surface friction (eq 12). This increases the energy conversion efficiency ε, defined as the ratio between the output and the input power. For pressure driven flow, ε is given by

$$\varepsilon = \frac{I\nabla\psi}{Q\Delta p} \tag{28}$$

where $\nabla\psi$ is the voltage gradient. Figure 4A shows the streaming current as a function of the water contact angle or the slip length (eq 10). The increase in the energy conversion efficiency for constant input pressure is shown in Figure 4B. For the micron-sized channels, the conversion efficiency can be increased by a factor of 1.4 using hydrophobic surface coatings as confirmed by our experiments (Figure 5). A further increase in the conversion efficiency could become possible by using nanofluidic channels that are comparable in size to the slip length.[30]

Guided by the theoretical predictions, we have employed surface coatings to vary the surface charge density and surface

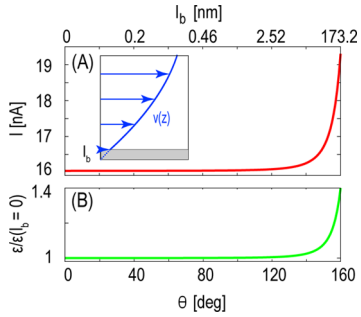

Figure 4. (A) Streaming current as function the surface hydrophobicity measured by the water contact angle Θ or the slip length l_b for constant input pressure. The inset shows a sketch of the slip velocity next to an interface. The slip length l_b corresponds to the distance wherein the linear extrapolation of the velocity profile reaches zero. (B) Efficiency increase by increasing the surface hydrophobicity at constant input pressure for a 30 μm channel with surface charge density of $\sigma = -0.0001$ e/nm^2.

DOI: 10.1021/acs.jpcc.6b03788
J. Phys. Chem. C 2016, 120, 14513−14521

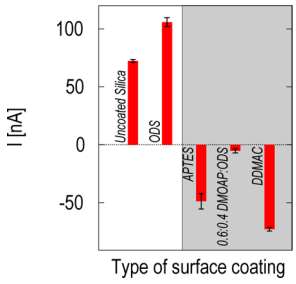

Figure 5. Streaming currents measured for surface coatings of varying surface charge density and surface hydrophobicity: Coating with ODS results in a negatively charged hydrophobic surface and increases the streaming current. The APTES and DDMAC coatings result in positively charged surfaces and reversal of the sign of the streaming current. The 0.6:0.4 DMOAP:ODS coating significantly reduces the surface charge density and thereby results in a large reduction in the streaming current. The gray area indicates reversal of the sign of the streaming current.

hydrophobicity of the channels. The results are shown in Figure 5 for a 30 μm channel. Reversal of the surface charge density and the sign of the streaming current is achieved by coating with APTES and DDMAC. Additionally, in agreement with the theoretical predictions, the streaming current increases with enhanced surface hydrophobicity. The ODS and DDMAC coatings are both terminated with long alkyl chains and thereby significantly reduce the hydrophilicity of the silica substrate. These two coatings significantly enhance the streaming current relative to that of their hydrophilic counterparts: uncoated silica (46.3%) and APTES (49.3%). Finally, a 0.6:0.4 mixture by mole ratio of DMOAP:ODS significantly reduces the surface charge density and therefore results in a much smaller streaming current.

CONCLUSIONS

In this work, we study electrokinetic streaming currents generated from water flowing through micron-sized channels, focusing on modifications of surface properties with the goal of increasing the energy conversion efficiency. The combination of a Poisson−Boltzmann description, continuum hydrodynamics, and microjet electrokinetic experiments provides detailed insight into the contribution of electrostatic and nonelectrostatic interactions to the streaming current. Specific adsorption of hydronium and hydroxide leads to anomalous ion-specific electrokinetic effects at *uncharged* surfaces, resulting in a streaming current of ∼1.8 pA. This nonelectrostatic contribution is negligible when compared to the contribution of long-ranged electrostatic interactions at *charged* surfaces, which result in streaming currents that are orders of magnitude larger (10−100 nA). In a negatively charged channel, the streaming current originates from the extended double layer formed from electrostatic interactions and by the preferential adsorption of hydronium to the solid/liquid interface. This more detailed model revises that suggested by Duffin et al., which proposed that hydroxide was preferentially adsorbed to the channel walls and the sole cause of the streaming current.[1,2] This previous model neglected to account for the channel's negative surface charge density. Specific ion adsorption becomes important for ions with high surface affinity ($V_S \gg k_BT$), and the interfacial affinity can be quantified using ultradilute salt solutions.

Tuning the surface properties of the channel, via silanization, provides a method for reversing the surface charge, thereby reversing the sign of the streaming current and switching between hydronium or hydroxide as the main charge carrier. Similarly, tuning the surface coating such that the surface charges are minimized results in a significant reduction in the streaming current, an effect that can be exploited to minimize interference by the streaming potential in liquid microjet X-ray and UV photoemission spectroscopy experiments.[57−59] Moreover, increasing the surface hydrophobicity provides an avenue for increasing the energy conversion efficiency by reducing dissipation from fluid/surface friction. In particular, using carbon nanotubes that are known to have an extremely large slip length could increase the current to a multiple of its current levels. However, generating a hydrostatic pressure differential at such small scales may prove challenging.

AUTHOR INFORMATION

Corresponding Authors

*E-mail: nschwierz@berkeley.edu.

*E-mail: saykally@berkeley.edu. Phone: 510-642-8269. Fax: 510-642-8369.

Author Contributions

[§]These authors contributed equally to this work.

Notes

The authors declare no competing financial interest.

ACKNOWLEDGMENTS

N.S. thanks the Alexander von Humboldt Foundation for financial support. The early stages of this work were supported by a grant from the NSF EAGER Program (Grant CHE-0963844). R.K.L. was supported by the Director, Office of Basic Energy Sciences, Office of Science, U.S. Department of Energy (DOE) under Contract No. DE-AC02-05CH11231, through the Chemical Sciences Division and Material Sciences Division of the Lawrence Berkeley National Laboratory (LBNL).

REFERENCES

(1) Duffin, A. M.; Saykally, R. J. Electrokinetic Hydrogen Generation from Liquid Water Microjets. *J. Phys. Chem. C* **2007**, *111*, 12031−12037.

(2) Duffin, A. M.; Saykally, R. J. Electrokinetic Power Generation from Liquid Water Microjets. *J. Phys. Chem. C* **2008**, *112*, 17018−17022.

(3) Faubel, M.; Steiner, B. Strong Bipolar Electrokinetic Charging of Thin Liquid Jets Emerging from 10 μm PtIr Nozzles. *Ber. Bunsenges. Phys. Chem.* **1992**, *96*, 1167−1172.

(4) Holstein, W. L.; Hayes, L. J.; Robinson, E. M. C.; Laurence, G. S.; Buntine, M. A. Aspects of Electrokinetic Charging in Liquid Microjets. *J. Phys. Chem. B* **1999**, *103*, 3035−3042.

(5) Groves, J. N.; Sears, A. R. Alternating Streaming Current Measurements. *J. Colloid Interface Sci.* **1975**, *53*, 83−89.

(6) Hummer, G.; Rasaiah, J.; Noworyta, J. Water Conduction Through the Hydrophobic Channel of a Carbon Nanotube. *Nature* **2001**, *414*, 188−190.

(7) Yang, J.; Lu, F.; Kostiuk, L.; Kwok, D. Electrokinetic Microchannel Battery by Means of Electrokinetic and Microfluidic Phenomena. *J. Micromech. Microeng.* **2003**, *13*, 963−970.

(8) Siria, A.; Poncharal, P.; Biance, A.-L.; Fulcrand, R.; Blase, X.; Purcell, S. T.; Bocquet, L. Giant Osmotic Energy Conversion Measured in a Single Transmembrane Boron Nitride Nanotube. *Nature* **2013**, *494*, 455−458.

(9) Chang, C.-C.; Yang, R.-J. Electrokinetic Energy Conversion Efficiency in Ion-Selective Nanopores. *Appl. Phys. Lett.* **2011**, *99*, 083102.

DOI: 10.1021/acs.jpcc.6b03788
J. Phys. Chem. C 2016, 120, 14513−14521

(10) van der Heyden, F. H. J.; Bonthuis, D. J.; Stein, D.; Meyer, C.; Dekker, C. Power Generation by Pressure-Driven Transport of Ions in Nanofluidic Channels. *Nano Lett.* **2007**, *7*, 1022−1025.
(11) van der Heyden, F. H. J.; Bonthuis, D. J.; Stein, D.; Meyer, C.; Dekker, C. Electrokinetic Energy Conversion Efficiency in Nanofluidic Channels. *Nano Lett.* **2006**, *6*, 2232−2237.
(12) Delgado, A. V.; González-Caballero, F.; Hunter, R. J.; Koopal, L. K.; Lyklema, J. Measurement and Interpretation of Electrokinetic Phenomena (IUPAC Technical Report). *Pure Appl. Chem.* **2005**, *77*, 1753−1805.
(13) Canning, J.; Buckley, E.; Huntington, S.; Lyytikäinen, K. Using Multi-Microchannel Capillaries for Determination of the Zeta Potential of a Microfluidic Channel. *Electrochim. Acta* **2004**, *49*, 3581−3586.
(14) Canning, J.; Buckley, E.; Lyytikainen, K. Electrokinetic Air-Silica Structured Multi-Microchannel Capillary Batteries. *Electron. Lett.* **2004**, *40*, 298−299.
(15) Yang, J.; Lu, F.; Kostiuk, L. W.; Kwok, D. Y. Electrokinetic Microchannel Battery by Means of Electrokinetic and Microfluidic Phenomena. *J. Micromech. Microeng.* **2003**, *13*, 963−970.
(16) Werner, C.; Körber, H.; Zimmermann, R.; Dukhin, S.; Jacobasch, H. Extended Electrokinetic Characterization of Flat Solid Surfaces. *J. Colloid Interface Sci.* **1998**, *208*, 329−346.
(17) Davidson, C.; Xuan, X. Effects of Stern Layer Conductance on Electrokinetic Energy Conversion in Nanofluidic Channels. *Electrophoresis* **2008**, *29*, 1125−1130.
(18) Werner, C.; Zimmermann, R.; Kratzmüller, T. Streaming Potential and Streaming Current Measurements at Planar Solid/Liquid Interfaces for Simultaneous Determination of Zeta Potential and Surface Conductivity. *Colloids Surf., A* **2001**, *192*, 205−213.
(19) Xie, Y.; Bos, D.; de Vreede, L. J.; de Boer, H. L.; van der Meulen, M.-J.; Versluis, M.; Sprenkels, A. J.; van den Berg, A.; Eijkel, J. C. T. High-Efficiency Ballistic Electrostatic Generator using Microdroplets. *Nat. Commun.* **2014**, *5*, 3575.
(20) Huang, D. M.; Cottin-Bizonne, C.; Ybert, C.; Bocquet, L. Ion-Specific Anomalous Electrokinetic Effects in Hydrophobic Nanochannels. *Phys. Rev. Lett.* **2007**, *98*, 177801.
(21) White, F. M. *Fluid Mechanics*, 4th ed.; McGraw-Hill: Boston, 1999.
(22) Davies, J. T.; Rideal, E. K. *Interfacial Phenomena*, 2nd ed.; Academic Press: New York, 1961.
(23) Rouse, H.; Howe, J. W. *Basic Mechanics of Fluids*, 2nd ed.; John Wiley & Sons, Inc.: London, 1953.
(24) Evans, D. F.; Wennerström, H. *The Colloidal Domain: Where Physics, Chemistry, Biology and Technology Meet*, 2nd ed.; Wiley-VCH: New York, 1999.
(25) Bocquet, L.; Charlaix, E. Nanofluidics, from Bulk to Interfaces. *Chem. Soc. Rev.* **2010**, *39*, 1073−1095.
(26) Bocquet, L.; Barrat, J.-L. Flow Boundary Conditions from Nano- to Micro-Scales. *Soft Matter* **2007**, *3*, 685−693.
(27) Huang, D. M.; Sendner, C.; Horinek, D.; Netz, R. R.; Bocquet, L. Water Slippage versus Contact Angle: A Quasiuniversal Relationship. *Phys. Rev. Lett.* **2008**, *101*, 226101.
(28) Sendner, C.; Horinek, D.; Bocquet, L.; Netz, R. R. Interfacial Water at Hydrophobic and Hydrophilic Surfaces: Slip, Viscosity, and Diffusion. *Langmuir* **2009**, *25*, 10768−10781.
(29) Bonthuis, D. J.; Netz, R. R. Unraveling the Combined Effects of Dielectric and Viscosity Profiles on Surface Capacitance, Electro-Osmotic Mobility, and Electric Surface Conductivity. *Langmuir* **2012**, *28*, 16049−16059.
(30) Bonthuis, D. J.; Rinne, K. F.; Falk, K.; Nadir Kaplan, C.; Horinek, D.; Nihat Berker, A.; Bocquet, L.; Netz, R. R. Theory and Simulations of Water Flow through Carbon Nanotubes: Prospects and Pitfalls. *J. Phys.: Condens. Matter* **2011**, *23*, 184110.
(31) Majumder, M.; Chopra, N.; Andrews, R.; Hinds, B. J. Nanoscale Hydrodynamics: Enhanced Flow in Carbon Nanotubes. *Nature* **2005**, *438*, 44.
(32) Luo, G.; Malkova, S.; Yoon, J.; Schultz, D. G.; Lin, B.; Meron, M.; Benjamin, I.; Vanysek, P.; Schlossman, M. L. Ion Distributions Near a Liquid-Liquid Interface. *Science* **2006**, *311*, 216−218.
(33) Boström, M.; Tavares, F.; Finet, S.; Skouri-Panet, F.; Tardieu, A.; Ninham, B. Why Forces Between Proteins Follow Different Hofmeister Series for pH Above and Below Pi. *Biophys. Chem.* **2005**, *117*, 217−224.
(34) Schwierz, N.; Netz, R. R. Effective Interaction between Two Ion-Adsorbing Plates: Hofmeister Series and Salting-In/Salting-Out Phase Diagrams from a Global Mean-Field Analysis. *Langmuir* **2012**, *28*, 3881−3886.
(35) Schwierz, N.; Horinek, D.; Sivan, U.; Netz, R. R. Reversed Hofmeister Series - the Rule rather than the Exception. *Curr. Opin. Colloid Interface Sci.* **2016**, *23*, 10−18.
(36) Schwierz, N.; Horinek, D.; Netz, R. R. Anionic and Cationic Hofmeister Effects on Hydrophobic and Hydrophilic Surfaces. *Langmuir* **2013**, *29*, 2602−2614.
(37) Borukhov, I.; Andelman, D.; Orland, H. Polyelectrolyte Solutions between Charged Surfaces. *Europhys. Lett.* **1995**, *32*, 499−504.
(38) Borukhov, I.; Andelman, D.; Orland, H. Steric Effects in Electrolytes: A Modified Poisson-Boltzmann Equation. *Phys. Rev. Lett.* **1997**, *79*, 435−438.
(39) Pegram, L. M.; Record, M. T. Partitioning of Atmospherically Relevant Ions Between Bulk Water and the Water/Vapor Interface. *Proc. Natl. Acad. Sci. U. S. A.* **2006**, *103*, 14278−14281.
(40) Schwierz, N.; Horinek, D.; Netz, R. R. Reversed Anionic Hofmeister Series: The Interplay of Surface Charge and Surface Polarity. *Langmuir* **2010**, *26*, 7370−7379.
(41) Saykally, R. J. Air/Water Interface: Two Sides of the Acid-Base Story. *Nat. Chem.* **2013**, *5*, 82−84.
(42) Pegram, L. M.; Record, M. T., Jr. Quantifying Accumulation or Exclusion of H^+, HO^-, and Hofmeister Salt Ions Near Interfaces. *Chem. Phys. Lett.* **2008**, *467*, 1−8.
(43) Mucha, M.; Frigato, T.; Levering, L. M.; Allen, H. C.; Tobias, D. J.; Dang, L. X.; Jungwirth, P. Unified Molecular Picture of the Surfaces of Aqueous Acid, Base, and Salt Solutions. *J. Phys. Chem. B* **2005**, *109*, 7617−7623.
(44) Buch, V.; Milet, A.; Vácha, R.; Jungwirth, P.; Devlin, J. P. Water Surface is Acidic. *Proc. Natl. Acad. Sci. U. S. A.* **2007**, *104*, 7342−7347.
(45) Tse, Y.-L. S.; Chen, C.; Lindberg, G. E.; Kumar, R.; Voth, G. A. Propensity of Hydrated Excess Protons and Hydroxide Anions for the Air-Water Interface. *J. Am. Chem. Soc.* **2015**, *137*, 12610−12616.
(46) Petersen, P. B.; Saykally, R. J. Is the Liquid Water Surface Basic or Acidic? Macroscopic vs. Molecular-scale Investigations. *Chem. Phys. Lett.* **2008**, *458*, 255−261.
(47) Yamaguchi, S.; Kundu, A.; Sen, P.; Tahara, T. Communication: Quantitative Estimate of the Water Surface pH using Heterodyne-detected Electronic Sum Frequency Generation. *J. Chem. Phys.* **2012**, *137*, 151101.
(48) Winter, B.; Faubel, M.; Vácha, R.; Jungwirth, P. Behavior of Hydroxide at the Water/Vapor Interface. *Chem. Phys. Lett.* **2009**, *474*, 241−247.
(49) Takahashi, M. ζ Potential of Microbubbles in Aqueous Solutions: Electrical Properties of the Gas-Water Interface. *J. Phys. Chem. B* **2005**, *109*, 21858−21864.
(50) Beattie, J. K.; Djerdjev, A. M.; Warr, G. G. The Surface of Neat Water is Basic. *Faraday Discuss.* **2009**, *141*, 31−39.
(51) Mishra, H.; Enami, S.; Nielsen, R. J.; Stewart, L. A.; Hoffmann, M. R.; Goddard, W. A.; Colussi, A. J. Brønsted Basicity of the Air-Water Interface. *Proc. Natl. Acad. Sci. U. S. A.* **2012**, *109*, 18679−18683.
(52) Baer, M. D.; Kuo, I.-F. W.; Tobias, D. J.; Mundy, C. J. Toward a Unified Picture of the Water Self-Ions at the Air-Water Interface: A Density Functional Theory Perspective. *J. Phys. Chem. B* **2014**, *118*, 8364−8372.
(53) Kelly, D. N.; Lam, R. K.; Duffin, A. M.; Saykally, R. J. Exploring Solid/Aqueous Interfaces with Ultradilute Electrokinetic Analysis of Liquid Microjets. *J. Phys. Chem. C* **2013**, *117*, 12702−12706.

DOI: 10.1021/acs.jpcc.6b03788
J. Phys. Chem. C 2016, 120, 14513−14521

(54) Behrens, S. H.; Grier, D. G. The Charge of Glass and Silica Surfaces. *J. Chem. Phys.* **2001**, *115*, 6716−6721.
(55) Schwierz, N.; Horinek, D.; Netz, R. R. Specific Ion Binding to Carboxylic Surface Groups and the pH Dependence of the Hofmeister Series. *Langmuir* **2015**, *31*, 215−225.
(56) de Gennes, P. G. On Fluid/Wall Slippage. *Langmuir* **2002**, *18*, 3413−3414.
(57) Faubel, M.; Steiner, B.; Toennies, J. Measurement of He I Photoelectron Spectra of Liquid Water, Formamide and Ethylene Glycol in Fast-Flowing Microjets. *J. Electron Spectrosc. Relat. Phenom.* **1998**, *95*, 159−169.
(58) Horio, T.; Shen, H.; Adachi, S.; Suzuki, T. Photoelectron Spectra of Solvated Electrons in Bulk Water, Methanol, and Ethanol. *Chem. Phys. Lett.* **2012**, *535*, 12−16.
(59) Shreve, A. T.; Elkins, M. H.; Neumark, D. M. Photoelectron Spectroscopy of Solvated Electrons in Alcohol and Acetonitrile Microjets. *Chem. Sci.* **2013**, *4*, 1633−1639.

DOI: 10.1021/acs.jpcc.6b03788
J. Phys. Chem. C 2016, 120, 14513−14521